

## Full length article

# Simultaneous determination of the lattice thermal conductivity and grain/grain thermal resistance in polycrystalline diamond



J. Anaya <sup>a</sup>, T. Bai <sup>b</sup>, Y. Wang <sup>b</sup>, C. Li <sup>b</sup>, M. Goorsky <sup>b</sup>, T.L. Bougher <sup>c</sup>, L. Yates <sup>c</sup>, Z. Cheng <sup>c</sup>, S. Graham <sup>c</sup>, K.D. Hobart <sup>d</sup>, T.I. Feygelson <sup>d</sup>, M.J. Tadjer <sup>d</sup>, T.J. Anderson <sup>d</sup>, B.B. Pate <sup>d</sup>, M. Kuball <sup>a,\*</sup>

<sup>a</sup> Center for Device Thermography and Reliability (CDTR), University of Bristol, Bristol B8 1TL, United Kingdom

<sup>b</sup> Materials Science and Engineering, University of California Los Angeles, CA 90095, USA

<sup>c</sup> George W. Woodruff School of Mechanical Engineering, Georgia Institute of Technology, Atlanta, GA 30313, USA

<sup>d</sup> Naval Research Laboratory, 4555 Overlook Ave SW, Washington, DC 20375, USA

## ARTICLE INFO

## Article history:

Received 30 March 2017

Received in revised form

3 August 2017

Accepted 4 August 2017

Available online 9 August 2017

## Keywords:

Thermal conductivity

Nanocrystalline diamond

Grain boundaries

## ABSTRACT

The in-plane and cross-plane thermal conductivity of polycrystalline diamond near its nucleation region have been measured by Raman thermography assisted by TiO<sub>2</sub> nanoparticles and by picosecond time-domain thermoreflectance (TDTR). This information has been combined with a finite element thermal model making use of the real grain structure, including information on the grain orientation, of the film extracted by transmission electron microscopy (TEM). This methodology allows to simultaneously determine the thermal resistance between grains and the lattice thermal conductivity of the sample without any adjustable parameter. The results show that the lattice thermal conductivity of the near nucleation diamond is 5–8 times smaller than the one observed in IIa single-crystalline diamond; the thermal resistance between grains is at least one order of magnitude higher than values predicted by molecular dynamic simulations. Finally, we show how the anisotropy in thermal conductivity observed in polycrystalline diamond naturally emerges from its grain structure and the thermal resistance at grain boundaries.

© 2017 The Authors. Published by Elsevier Ltd on behalf of Acta Materialia Inc. This is an open access article under the CC BY license (<http://creativecommons.org/licenses/by/4.0/>).

## 1. Introduction

The high thermal conductivity of diamond (up to 3300 W/mK) has been widely exploited in thermal management of different applications, e.g. high power lasers [1], high power light emitting diodes (LEDs) [2], x-ray optical windows [3] and high power electronic devices [4]. In all of these applications, and because nowadays polycrystalline diamond can reach thermal conductivities approaching those of single crystal diamond, polycrystalline rather than single crystalline diamond is used without any detriment [5]. However, for achieving this performance polycrystalline diamond needs to be polished removing the material of the first microns of growth corresponding to the near nucleation diamond [6]. In this region, comprising the first microns of diamond from nucleation, the thermal conductivity is much lower than bulk values; it is also

anisotropic i.e. cross-plane and in-plane thermal conductivity differ in value; the thermal conductivity also shows a strong dependence on the average grain size [6–8]. Due to the difficulty of measuring the thermal properties of ultra-thin diamond films, the thermal transport in this region of the diamond has been scarcely studied, and the existent data reported in the literature show significant disparity in values [8]. However, the recent integration of diamond with GaN high electron mobility transistors (HEMTs) has revived the interest in a better understanding of the diamond properties in this near-nucleation region, since a low thermal conductivity in this region may be a bottleneck for this technology [9–11]. It should be noted that the thermal conductivity values reported in the literature for ultrathin diamond layers (<3 μm) range from a few tens to few hundreds of W/mK [8,12–15], with cross plane/in-plane anisotropy rates ranging from 1.5 up to 20 [6,8,13–15]. To explain these low thermal conductivity values, two main factors have typically been considered: the low quality of the diamond lattice in this region, and the presence of grain boundaries acting as thermal barriers [6,8,13–15]. The latter has also been qualitatively used to

\* Corresponding author.

E-mail address: [martin.kuball@bristol.ac.uk](mailto:martin.kuball@bristol.ac.uk) (M. Kuball).

justify the anisotropy in thermal conductivity due to the characteristic columnar shape of the polycrystalline diamond grains [6,8]. However, while these two factors undoubtedly impact the heat transport in the near nucleation diamond region, still it is poorly understood how to quantify their individual contribution to the reduction of thermal conductivity and how they are related to the emergence of anisotropy in the heat conduction.

Typically the quality of the lattice in polycrystalline diamond is typically explored by means of its Raman signal [16]. When approaching the near nucleation diamond it is common to observe features attributed to a low-quality lattice: the  $sp^3$  diamond peak becomes broader than for single crystal/bulk CVD diamond, and other features appear in the Raman spectrum apart of the diamond Raman peak ( $sp^2$  bonds, transpolyacetylene peaks, etc.) [16,17]. However, while this is clear evidence for a somewhat less crystalline lattice structure, it says little about whether these contributions to the Raman spectra arise from the in-grain lattice or from the grain boundaries regions, which are prone to accumulate defects including  $sp^2$  and  $CH_x$  bonds [18,19]. On the other hand, theoretical values computed from molecular dynamics simulations have shown that the thermal resistance between perfect grain boundaries in polycrystalline diamond range between 0.02 and 0.1  $m^2K/GW$  depending on its mismatch angle [20,21]. On the other hand, reported literature values for this magnitude from experimental measurements are much higher, on the order of 0.5–3  $m^2K/GW$  [7,12,21], which can only be explained by a significant accumulation of defects/disorder at and near the grain boundaries [20]. It is worth noting that experimental values of grain/grain thermal resistance are typically extracted indirectly from experimental data. For this, models make use of strong simplifications, for example, bulk-like in-grain thermal conductivities [12,21] and a single average value for the in-plane grain size (in the case of the columnar grains those may be somewhat arbitrary due to the lack of regularity) are considered [8]. In any case, how the grain/grain thermal resistance correlates with the cross-plane thermal conductivity, and therefore the thermal conductivity anisotropy factor, is still poorly understood, and at best only approached by simplified models making use of indirect phenomenological relations [6].

To shed some light on this problem, we demonstrate in this work a methodology able to unravel the individual roles of grain boundaries and lattice thermal conductivity on the thermal transport in the near nucleation site of polycrystalline diamond. For this, we have determined the in-plane and cross-plane thermal conductivity experimentally in a polycrystalline diamond thin film (1  $\mu m$  thick). This has been combined with thermal simulations making use of the real grain structure, including grain orientation, of the sample, which was determined by transmission emission microscopy (TEM). Using this methodology the in grain thermal conductivity and thermal resistance between grains can be simultaneously determined from both cross-plane and in-plane measurements without any fitting parameters.

## 2. Experimental details

Diamond films of about 1  $\mu m$  thickness were deposited on 200  $\mu m$  thick silicon substrates by microwave plasma-assisted chemical vapor deposition (MPCVD) in an IPLAS 5.0 KW CVD reactor with hydrogen and methane as reactant gases. The substrate temperature and chamber pressure were kept constant throughout the entire diamond film growth and remained at 750 °C and 7.08 torr respectively. The microwave power and methane to hydrogen ratio was varied, respectively, from 800 W to 0.5% during the initial 20 min of film growth to 1400 W and 0.7% through the continuing diamond deposition. The diamond film thickness was

measured by in situ laser reflectometry. Prior to growth, the silicon substrate was seeded by ultrasonic treatment in ethanol-based nanodiamond suspension prepared from detonation nanodiamond powder which was acquired from International Technology Center, North Carolina, USA (ITC). According to the manufacturer specifications the material grade used here has a high degree of grain size homogeneity with an average particle size of 4 nm, and a chemical purity in excess of 98%. Scanning electron microscopy analysis (SEM) of the back side of a typical diamond film deposited with above mentioned seeding method shows a uniform nucleation with seed density greater than  $10^{12}$  nuclei/cm<sup>2</sup>. In general, the use of carbon-lean growth conditions is intended to suppress secondary renucleation, and increases film quality by decreasing grain/boundary ratio. Such diamond films are basically formed through the grain coalescence and subsequent growth competition of initially random oriented nanodiamond seeds. The orientation of crystallites fastest growth direction in relation to substrate surface is the key to seeds survival. Only the crystallites with fastest growth direction nearest to normal to the growth surface survive at the end. This ultimately leads to a formation of a well pronounced columnar grain structure in the film, as well as an increase in lateral grain size with film thickness.

The structural characterization included electron microscopy x-ray scattering techniques. Electron transparent plan view and cross section samples were prepared using a focused ion beam instrument (Nova 600 FIB). SEM images of the diamond surface morphology were also produced using the FIB instrument. Transmission electron microscopy (TEM) images were generated using a Titan S/TEM (FEI) system under 200 kV. The scanning transmission electron microscopy (STEM) mode allows to analyze the grain size distribution while the high angle annular dark field (HAADF) detector in the STEM mode provides contrast based on the differences in the adjacent grain orientation and distinguishes clearly between grain boundaries and twins. The orientation of the different grains was quantified using two techniques. First, selected area electron diffraction (SAED) patterns were used to produce images of grains with specific orientations. Tilting the sample imaged different grains, so the relative misorientation between adjacent grains could be estimated. The second approach was to employ precession electron diffraction (PED) mapping with a 10 nm step size from which the orientation of each grain is mapped using a color-coded legend. X-ray scattering measurements utilized a Jordan Valley D1 ( $CuK_{\alpha}$  radiation) with incident parallel beam optics for both  $2\theta:\omega$  scans and pole figures using Soller slits. Full pole figure data were collected with a fixed diffraction angle  $2\theta$  by varying the tilt angle with respect to the sample surface normal direction ( $\chi$ ) from 0° to 80° with a step size of 2° and rotation angle around sample surface normal direction ( $\varphi$ ) from 0° to 360° with a step size of 1°. Pole figures were plotted with the obtained diffracted intensity data as a function of  $\chi$  and  $\varphi$ .

For producing diamond membranes for in-plane thermal measurements, the silicon substrate was etched away by dry etching to obtain several  $460 \times 1000 \mu m$  freestanding diamond membranes similar to the ones described in Refs. [8,22]. Test structure designs consisted of metal heaters on these diamond membranes; this generates a temperature field in the freestanding diamond membrane when an electrical current flows through the line heater. The test structures were fabricated by first patterning 20 nm Cr followed by 300 nm Au by lift-off lithography. Diamond etching was performed by first depositing SiN by PECVD and patterning by ICP RIE using  $SF_6$ . Diamond was etched by RIE ICP  $O_2/Ar_2$  chemistry. The SiN mask was removed by a combination of RIE ICP and buffered HF. Diamond membranes were fabricated by Bosch etching of the Si wafer to produce deep vias stopping selectively on the diamond film.

### 3. Experimental measurement of the diamond microstructure

The in-plane grain size distribution, both using SEM and TEM, was determined using the standard intercept method [1] with four directions (0°, 45°, 90° and 135°) chosen to account for the non-equiaxed grains, as shown in Fig. 1. The average grain size obtained is 184 nm from the TEM plan view image (Fig. 1-a), and 240 nm from the SEM image (Fig. 1-b). It can be seen that the TEM image shows better contrast between different grains, and therefore displays the actual grain boundaries. On the other hand, in the SEM image, small grains without significant contrast difference do not show visible grain boundaries, and are typically regarded as part of another grain. The difference is demonstrated in the grain size distribution plots: the distribution using the SEM image (Fig. 1-c) shows larger grains with greater than 300 nm size, whereas the distribution determined from the TEM image (Fig. 1-d) shows a smaller average grain size and the presence of grains less than 120 nm in size. A more accurate determination of the grain distribution (using TEM) provides important input into the thermal analysis. Therefore, TEM approach will produce a more accurate grain size, while the SEM approach is more likely to overestimate the grain size. Fig. 1-e and 1-f correspond to PED orientation maps, the out-of-plane and in-plane orientation of each grain, respectively. Qualitatively, there are more grains with an out-of-plane orientation closer to (110) than other orientations, suggesting that the growth parameters favor a preferred out-of-plane (110) orientation. A comparison of the out-of-plane and in-plane orientations provides further insight into the grain orientations and sizes. At the left center of Fig. 1-e and Fig. 1-f is a region delineated by a thick black line. The out-of-plane image

(Fig. 1-e) indicates that this region has (110) orientation but the in-plane image (Fig. 1-f) shows that this region is actually comprised of an agglomeration of smaller grains with different in-plane orientation.

Fig. 2 shows the (220) and (111) pole figures of the diamond film. The x-ray beam illuminates a surface area of several mm<sup>2</sup> and therefore provides a better overall average of the film properties compared to the TEM measurements which includes a small number of grains. Note that a pole figure with a uniform color would indicate a random orientation of grains. Confirming the earlier results, Fig. 2-a shows that there is a preferred orientation of (110) grains (using the (220) reflection) oriented in the out-of-plane direction – corresponding to the central region of the figure. The (111) pole figure (Fig. 2-b), on the other hand, shows a reduced intensity in the center region and a ring of stronger intensity at ~35° from the central region. The (111) reflected intensity at this angle corresponds to those grains that have (110) planes parallel to the surface (the angle between (111) and (110) for a cubic crystal is 35.3° or 90°). This ‘ring’ of intensity is also relatively uniform in intensity, indicating that the in-plane orientations of the diamond grains are random.

The cross-section grain structure of the diamond film is shown by the STEM image in Fig. 2-a. The different grain orientations are observed through the grey-scale contrast and the elongated nature of the grains is evident. Twins are typically observed as straight-line boundaries of one contrast within a region of different contrast, as labeled in the figure. Also, near the silicon interface, the nucleation region is clearly observed by the presence of several nanoscale grains. The STEM image does provide a useful reference for the grain growth, presence of grain boundaries and twin boundaries, but the actual boundaries are delineated using a series of images

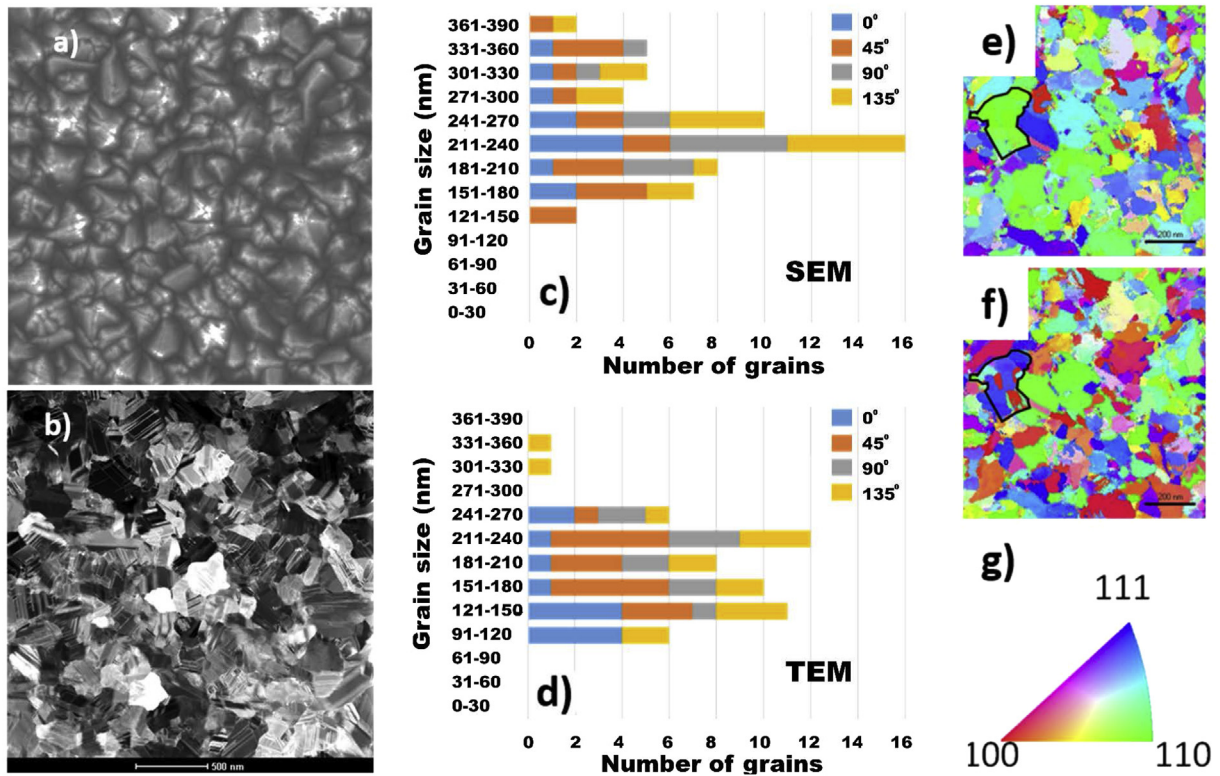
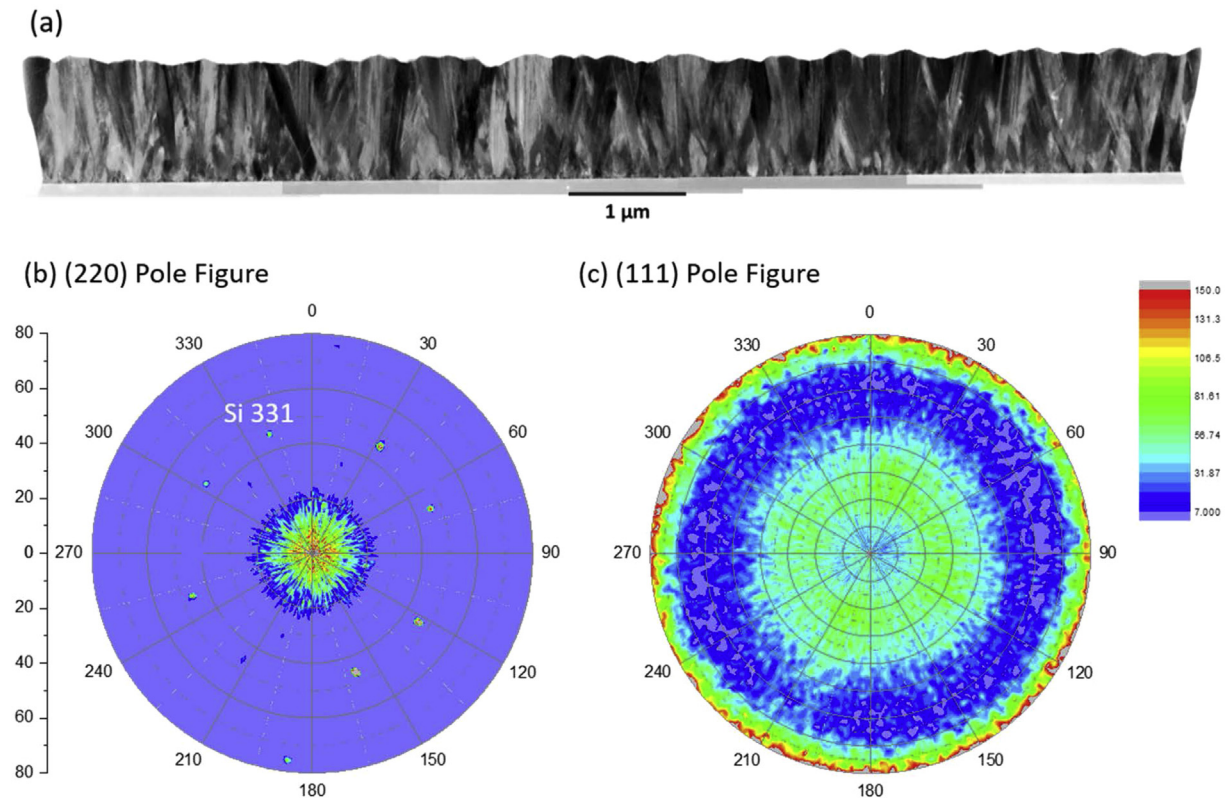


Fig. 1. (a) Plan view image of the measured diamond layer surface using SEM, and (b) from a STEM image extracted from the surface region of the diamond film. The scale bar shown in (b) is also the scale bar for (a). (c) Distribution of the grain dimension from the SEM image and (d) from TEM. (e,f) correspond to PED orientation maps with (g) providing the orientation legend.



**Fig. 2.** (a) Transversal TEM image showing the grains and stacking faults/twins in the diamond film studied. (b,c) pole figures showing preferential (110) orientation of the grains. Note also there are also eight points of intensity at  $46.5^\circ$  from the center. These correspond to the (331) planes from the Si substrate. The Bragg angle for the (331) Si reflection is within  $0.5^\circ$  of the diamond (220) so it is also captured in this measurement.

from SAED patterns and from PED measurements.

#### 4. Experimental measurement of the thermal conductivity: Raman and TDTR

To determine thermal conductivity, temperatures are measured at specific points in the diamond membranes by Raman thermography assisted by nanosensors to minimize errors [22]. For this, a variation of the technique described in Ref. [22] consisting of making use of  $\text{TiO}_2$  nanoparticles instead of Si NWs as Raman nanosensors has been used here.  $\text{TiO}_2$  nanoparticles with a purity of 99.98% (Anatase) and with an average size of 30 nm were sonicated in ethanol and deposited onto the sample by drop casting, keeping the sample above the ethanol boiling point to achieve a homogeneous deposition on the sample.  $\text{TiO}_2$  nanoparticles were selected as Raman nanosensors since they have a very strong Raman cross-section, high sensitivity to the temperature when using the  $E_g$   $143\text{ cm}^{-1}$  Raman peak and negligible phonon confinement effects above 20 nm nanoparticle size [23–25]. The Raman shift induced by the temperature field in the diamond membranes and  $\text{TiO}_2$  nanoparticles was acquired using a Renishaw InVia spectrometer making use of a 488 nm laser beam focused by a  $50\times$  (0.65NA) objective. The response to a temperature change of the  $E_g$   $143\text{ cm}^{-1}$  Raman shift was calibrated in a Linkam thermal stage for several nanoparticles, obtaining identical temperature response as the one reported in Ref. [24]. A 4-probe configuration was used to accurately monitor the electrical power dissipated in line heaters on the freestanding membranes; the thermal conductivity of the film was extracted by comparing the experimental temperature measurements with a finite element solution of the temperature field in the membrane. More details about this technique can be found in

Ref. [22]. Temperature profiles obtained across one of these freestanding membranes for two different powers together with the simultaneous fit from the finite element thermal simulation are shown in Fig. 3-a. Besides, the peak temperature in the center of the membrane versus the power dissipated in the heater is shown in Fig. 3-b. This was measured through Raman thermography on a  $\text{TiO}_2$  nanoparticle in the middle of the heater and additionally by monitoring the change in the resistance of the line heater with the temperature of the central part of the heater (see Fig. 3-b, inset). The perfect linear behavior observed in Fig. 3-b clearly shows that the thermal resistance of the diamond film does not change significantly in the 20–200 °C temperature range, and thus neither does its in-plane thermal conductivity. It should be noted that electrical measurements above 150 °C were not reliable, most likely due the intermixing of Au with the thin layer of Ti used as adhesion layer used for their fabrication; however, in the 25–150 °C range, an excellent agreement between the two methods was observed. Finally, the above-described measurements were repeated in more than 10 membranes distributed along the entire wafer, and an average value of  $95 \pm 10\text{ W/mK}$  was extracted for the in-plane thermal conductivity of this material. This value, while much lower than the one found in single crystal diamond, is in line with what has been previously reported for similar diamond thin films [8,22].

The through-plane thermal conductivity of the diamond film is measured using time domain thermoreflectance (TDTR), a well-established technique to measure the thermal conductivity and thermal boundary resistance of thin films. The experimental details of TDTR have been explained thoroughly elsewhere [26,27], but briefly TDTR is a pump and probe technique that utilizes an ultra-fast laser with a pulsewidth in the order of 1–10 ps to thermally

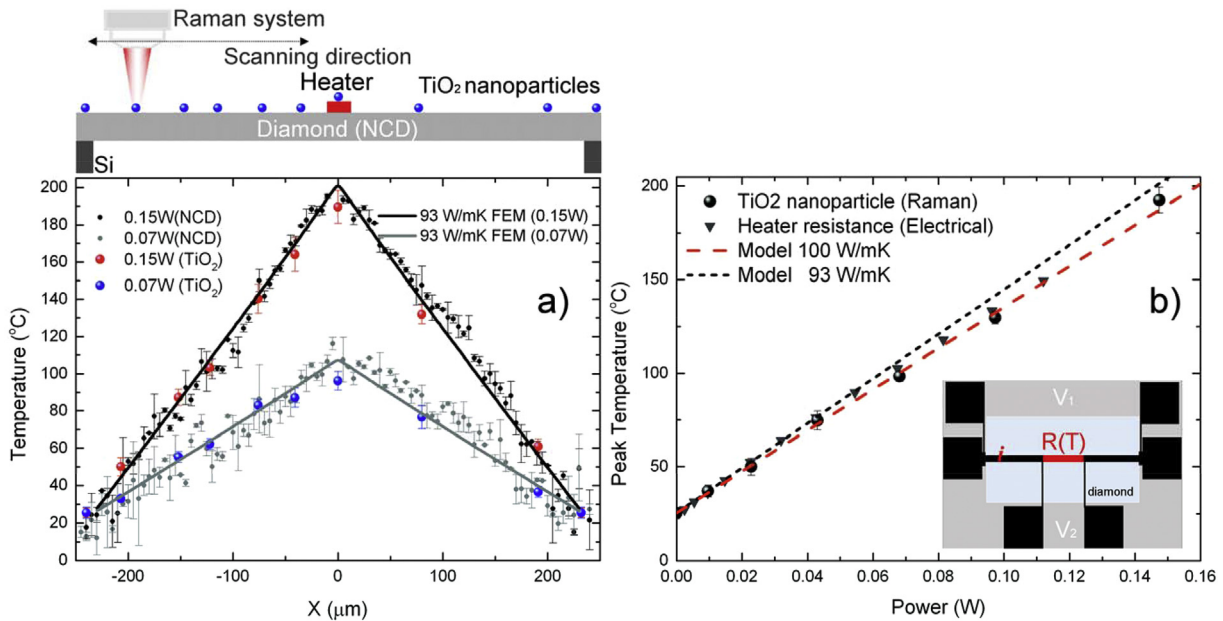


**Fig. 3.** Example of the in-plane thermal conductivity measurements performed on the measured diamond membrane. (a) Temperature profiles obtained from the diamond and TiO<sub>2</sub> nanoparticles on the freestanding diamond membrane (see sketch, top) for two different powers and its simultaneous fitting with 93 W/mK. (b) Temperature in the central region of the membrane (red area in inset illustrating sketch of heater and contact layout) vs power dissipated in the heater measured on TiO<sub>2</sub> nanoparticles and by electrical thermometry. (For interpretation of the references to colour in this figure legend, the reader is referred to the web version of this article.)

excite a sample, measure the temperature decay, and extract thermal properties using a diffusive heat conduction model over timescales from 0.1 to 7 ns. In our implementation of TDTR, we use a Ti:sapphire laser oscillating at 80 MHz at a wavelength of 800 nm. An electro-optic modulator (EOM) chops the pump pulse at a frequency between 1 and 12 MHz and the pump pulse is frequency-doubled to 400 nm in a BiBO crystal. The pump and probe beams impinge on the sample surface with perpendicular incidence; in this work we use a  $1/e^2$  beam diameter of 40 μm for the pump and 14 μm for the probe. Although for the beam sizes used the conduction is primarily one dimensional, the model accounting for radial conduction is used [27], and literature values are assumed for the different known material properties needed in the model (see Table 1).

A standard sample configuration for thin film thermal conductivity measurement by TDTR was used; the sample consisted of 90 nm of Al deposited on top of the diamond film on the Si substrate (measured by picosecond acoustics). The heating frequencies of 1–12 MHz fully penetrate the diamond layer so the measurement is also sensitive to the Si properties and the Si-diamond thermal boundary resistance. The three unknown parameters are the diamond through-plane thermal conductivity ( $\kappa_{dia}$ ), the Al-diamond thermal boundary resistance ( $TBR_{Al-dia}$ ), and the diamond-Si thermal boundary resistance ( $TBR_{dia-Si}$ ). We define the average sensitivity for a TDTR measurement as:

$$S_{p,avg} = \frac{1}{N} \sum_{i=1}^N \left| \frac{dR/R_i}{dp/P_i} \right| \quad (1)$$

where  $R$  is the measured ratio of in phase temperature signal to out

**Table 1**  
Material properties used for analysing the TDTR data. \* The Al thickness and thermal conductivity have been measured using picosecond acoustics and the Wiedemann Franz law.

	$\rho$ (Kg/m <sup>3</sup> )	$c_p$ (J/Kg)	Thickness ([μm])	$\kappa$ (W/m)
Al	2700	897	0.09*	175*
Si	2330	75	100	148
Diamond	3515	490	1.1	X

of phase temperature signal ( $-V_{in}/V_{out}$ ) and  $p$  is the value of the property of interest, and  $S_{p,i}$  is defined in previous literature [28,29]. The average sensitivity provides a single sensitivity value for the entire time region of measurement to allow direct comparison of the ability to resolve different unknown parameters with the measurement. Fig. 4-a shows the average sensitivity to the three unknown parameters in the measurement; the sensitivity to the thermal conductivity of the diamond layer is lower than that of the two interfaces because the diamond layer is relatively thin (~1 μm) and conductive (>150 W/m-K). We simultaneously fit for the three unknown parameters on the sample -namely, diamond cross-plane thermal conductivity, Al/Diamond thermal resistance ( $TBR_{Al-dia}$ ) and Diamond/Silicon thermal resistance ( $TBR_{dia-Si}$ ), using four different frequencies (Fig. 4-b). The uncertainties are calculated using a Monte Carlo simulation as described in Ref. [30], and the resulting diamond cross-plane thermal conductivity is  $175 + 65/-42$  W/m-K with  $TBR_{dia-Si}$  and  $TBR_{Al-dia}$  values of  $13.7 + 3.8/-3.5$  m<sup>2</sup>-K/GW, and  $5.6 + 0.6/-0.5$  m<sup>2</sup>-K/GW respectively. All these values are in the order of what has been reported in literature for similar thin diamond layers and similar interfacial thermal resistances [22,31,32]; however it should be noted that this properties are dependent on surface chemistry and growing conditions and therefore it is expected to find different values for different samples.

### 5. Modeling and data analysis

To analyze the thermal transport in this kind of diamond material typically the in-grain thermal conductivity (lattice thermal conductivity) of the grains and the quality of the grain boundaries needs to be considered. This is typically approached by the following well-known relationship [8].

$$\kappa = \frac{\kappa_{in-grain}}{1 + \frac{\kappa_{in-grain}}{d/R_{GB}}} \quad (2)$$

with  $\kappa_{in-grain}$  thermal conductivity of the grain lattice,  $d$  is the

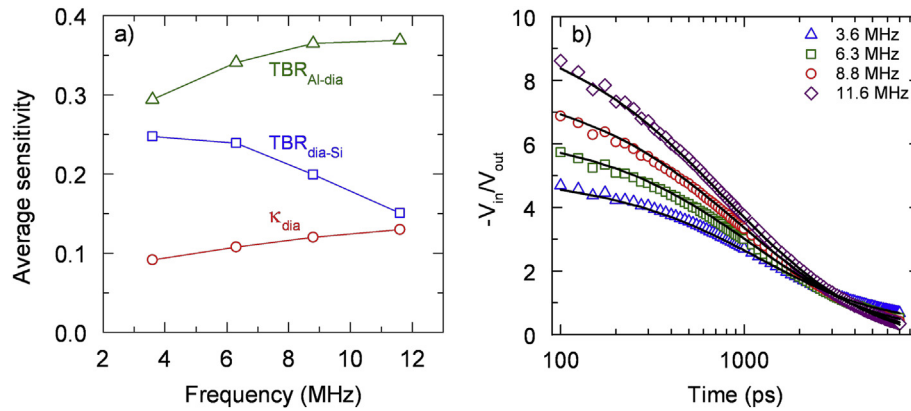


**Fig. 4.** Time domain thermoreflectance (TDTR) measurements: (a) Average sensitivity versus heating frequency for three unknown parameters: Diamond through-plane thermal conductivity ( $\kappa_{dia}$ ), Al-diamond thermal boundary resistance ( $TBR_{Al-dia}$ ), and diamond-Si thermal boundary resistance ( $TBR_{dia-Si}$ ). (b) Four-frequency fit for three unknown parameters on N3S-200-070815,  $\kappa_{dia} = 175 \pm 65/-42$ ,  $TBR_{dia-Si} = 13.7 \pm 3.8/-3.5$  m<sup>2</sup>-K/GW,  $TBR_{Al-dia} = 5.6 \pm 0.6/-0.5$  m<sup>2</sup>-K/GW.

average grain size, and  $R_{CB}$  is the thermal resistance between grains. This formalism has proven to be a good description when grains are regular in shape and the mean free path of the phonons in the lattice is smaller than the distance between grain boundaries [8]. However polycrystalline diamond shows a large disparity in grains sizes and also anisotropy in its geometry (see Figs. 1 and 2). Therefore determining a unique average value for  $d$  in the cross-plane and in-plane directions is somewhat arbitrary for this material and also may depend on the technique, SEM or TEM, used to unravel the structure. Besides in diamond, a great amount of heat is carried by long mean free path (MFP) phonons, which may result in

a lower  $\kappa_{in-grain}$  than the one found in single crystals when the crystallites are smaller than 1  $\mu\text{m}$  [8]. Hence the three parameters appearing in Eq. (2), namely  $\kappa_{in-grain} \cdot d$ , and  $R_{CB}$  must be determined from experimental data. Additionally, to explain with Eq. (2) the anisotropy observed from the in-plane and cross-plane measurements in an isotropic lattice, different values for  $d$  are needed. As a result an infinite number of combinations of  $\kappa_{in-grain}$ ,  $d$ , and  $R_{CB}$  may reproduce an experimentally determined thermal conductivity, and therefore little information can be obtained about the individual contribution of  $\kappa_{in-grain}$  and  $R_{CB}$  to the thermal resistance of the material from Eq. (2).

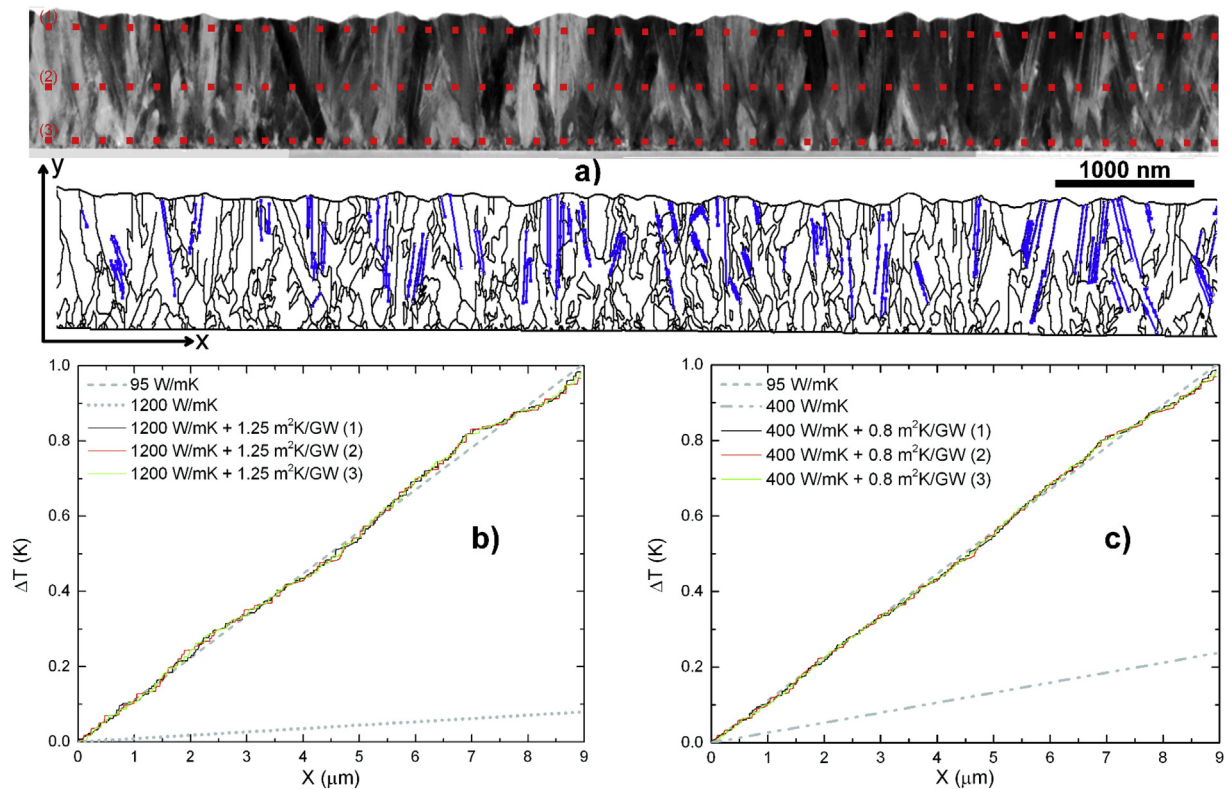


**Fig. 5.** (a) Grain structure of the film as determined from the TEM analysis. The twins detected in the film are remarked in blue. (b,c) Results of solving the in-plane heat equation (Eq. (2)) in this structure along the film a slab with no grain boundaries and when grain boundaries are considered for a lattice thermal conductivity of 1200 W/mK and 400 W/mK, respectively. Note that a material with 95 W/mK can be reproduced with different combinations of  $\kappa_{in-grain}$  and  $R_{CB}$ . (For interpretation of the references to colour in this figure legend, the reader is referred to the web version of this article.)

Here a different approach consisting of replicating the experiments by solving the heat equation on a long slab of material containing its real 2D grain structure, determined from the more accurate TEM technique, was used, thus removing the incertitude introduced by the average grain size. Since the material is relatively homogeneous in the growth plane (see Fig. 1), we can approximate the experimental values measured in the films by the in-plane and cross-plane  $k_{eff}$  values of the 2D slab, and thus, only  $k_{in-grain}$  and  $R_{GB}$  remain unknown. For this, the grain structure on a long slab of material of the diamond film determined by TEM (9  $\mu\text{m}$ , see Figs. 2-a and 5-a) was incorporated into a diffusive heat transport model implemented in COMSOL Multiphysics. The resulting geometry consists of more than 1000 grains of different shapes and sizes, containing more than 7500 boundaries in which the heat equation corresponding to an equivalent Raman (in-plane) and TDTR (cross-plane) thermal conductivity measurement experiments was solved. It should be noted that the magnitude of  $R_{GB}$  may depend on the orientation of the grains and the amount of defects that the boundaries accumulate [8,12,20,21]. However, since the grains are preferentially oriented (see Fig. 2), the effect of different orientations in  $R_{GB}$  can be neglected here in first approximation. On the other hand, while grain boundaries are prone to accumulate defects, increasing their thermal resistance, twins/stacking faults provide cleaner boundaries. Therefore we considered here different boundary conditions for real grain boundaries and for twins/stacking faults which at best can reach, following molecular dynamics simulations, thermal resistances of 0.06  $\text{m}^2\text{K}/\text{GW}$  [20].

To reproduce theoretically an equivalent steady state experiment as the one used experimentally for in-plane thermal conductivity measurements, a prescribed heat density was imposed as a boundary condition in one of the ends of the slab, while a fixed temperature was imposed into the other end. For this condition, the thermal conductivity ( $k_{eff}$ ) of a homogenous slab of material without interior boundaries can be easily determined from  $q_0 = k_{eff} \times \Delta T/L$ , where  $\Delta T$  is the temperature difference between the heat source ( $q_0$ ) and heat sink, and  $L$  is the separation between them. However, when the internal boundary conditions are considered the heat equation needs to be solved by finite elements subject to the following boundary conditions:

$$\begin{aligned}
 &-\nabla \cdot (\kappa(x,y)\nabla T(x,y)) = 0 \\
 &-n \cdot q = q_0 \text{ for } x = 0 \\
 &T = 20^\circ\text{C for } x = L \\
 &\begin{cases} -n_L \cdot q_L = -\frac{(T_R - T_L)}{R_{GB}}, -n_R \cdot q_R = -\frac{(T_L - T_R)}{R_{GB}} \text{ for grain boundaries} \\ -n_L \cdot q_L = -\frac{(T_R - T_L)}{R_{twin}}, -n_R \cdot q_R = -\frac{(T_L - T_R)}{R_{twin}} \text{ for twins} \end{cases} \\
 &-n \cdot q = 0 \text{ elsewhere}
 \end{aligned} \tag{3}$$

If no thermal resistance between grains is considered Eq. (3) gives the trivial solution in which  $k_{eff} = k_{in-grain}$ ; when the boundary condition for grain boundaries and twins in Eq. (3) is applied, then the value of  $k_{eff}$  is reduced from  $k_{in-grain}$  as  $R_{GB}$  increases (see Fig. 5). However, even having removed the incertitude introduced by the grain sizes, the experimental thermal conductivity can be reproduced with an infinite set of ( $k_{in-grain}, R_{GB}$ ) values. We illustrated this behavior in Fig. 5-b and 5-c, for two examples of these simulations using two values of  $k_{in-grain}$ , 1200 W/mK and 400 W/mK. To further reduce incertitude, and since these two parameters,  $k_{in-grain}$  and  $R_{boundary}$  are independent of the heat flow direction, we exploited the anisotropy detected experimentally to uniquely determine their value from simultaneously satisfying the in-plane thermal conductivity and cross-plane data in the 2D slab.

To reproduce an experiment similar to the one used for determining the cross-plane thermal conductivity, we created a transient simulation in the 2D slab containing the real grain structure of the film. For this, a homogeneous 100 nm thick layer was digitally added on top of the 2D slab to consider the Al transducer used in the TDTR experiments, and also a thick slab was added to the bottom of the geometry to take into account the Si substrate (see Fig. 6-top). The thermal resistance between these two layers and the diamond was included as boundary condition into the thermal model which was solved by finite elements subject to the following boundary conditions

$$\begin{aligned}
 &\rho c_p \frac{\partial T}{\partial t} - \nabla \cdot (\kappa(x,y)\nabla T(x,y)) = 0 \\
 &-n \cdot q = q_0 \times \exp\left(-\frac{(x-x_0)^2}{\sigma_x^2}\right) \times \exp\left(-\frac{(t-t_0)^2}{\sigma_t^2}\right) \text{ for } y = \text{top Al surface} \\
 &T = 20^\circ\text{C for } y = \text{bottom Si surface} \\
 &\begin{cases} -n_U \cdot q_U = -\frac{(T_U - T_D)}{R_{Al-Diamond}}, -n_D \cdot q_D = -\frac{(T_U - T_D)}{R_{Al-Diamond}} \text{ for Al/Diamond interface} \\ -n_U \cdot q_U = -\frac{(T_U - T_D)}{R_{Diamond-Si}}, -n_D \cdot q_D = -\frac{(T_U - T_D)}{R_{Diamond-Si}} \text{ for Diamond/Si interface} \end{cases} \\
 &\begin{cases} -n_L \cdot q_L = -\frac{(T_R - T_L)}{R_{GB}}, -n_R \cdot q_R = -\frac{(T_L - T_R)}{R_{GB}} \text{ for grain boundaries} \\ -n_L \cdot q_L = -\frac{(T_R - T_L)}{R_{twin}}, -n_R \cdot q_R = -\frac{(T_L - T_R)}{R_{twin}} \text{ for twins} \end{cases} \\
 &-n \cdot q = 0 \text{ elsewhere}
 \end{aligned} \tag{4}$$

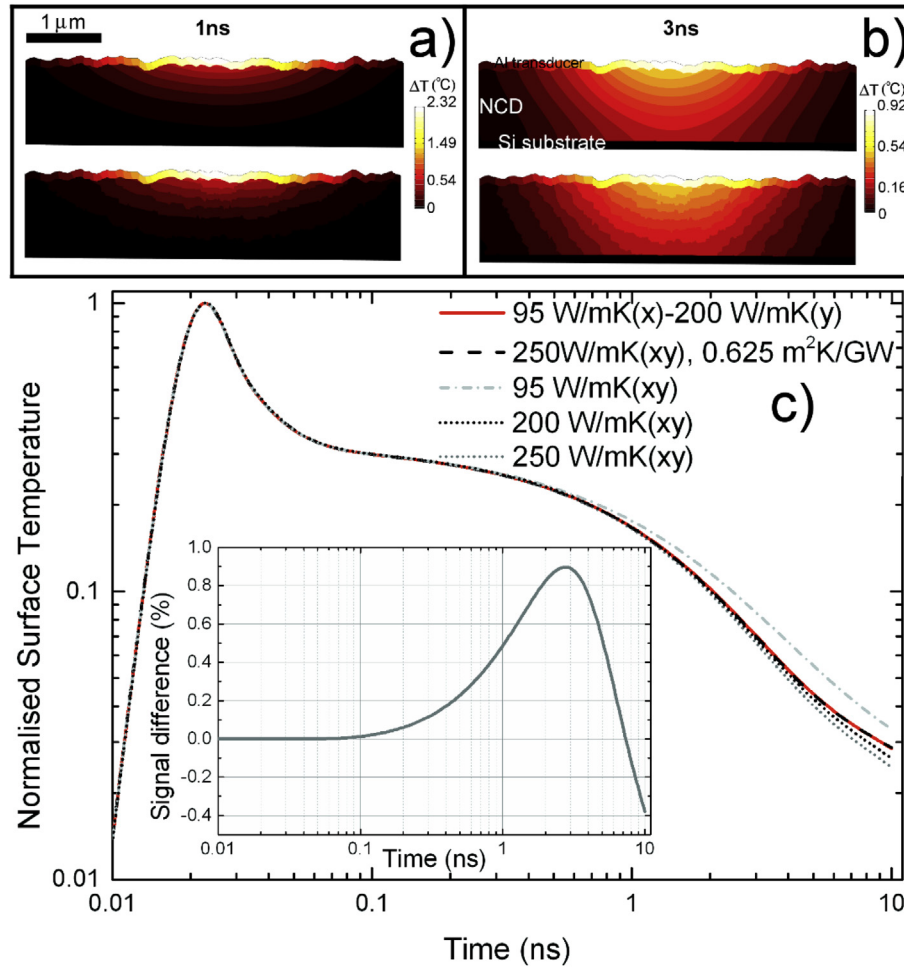


**Fig. 6.** (a,b) Penetration of the heat wave applied to the top of the diamond film (with a Si substrate underneath the film) in an anisotropic 2D slab without internal boundaries (top), and in a slab with isotropic thermal conductivity of individual grains with internal boundaries (bottom) at different times. (c) Transient average temperature of the transducer surface as used in a TDTR experiment for various diamond thermal conductivities. Note that an anisotropic thermal conductivity and a material with a homogeneous thermal conductivity and internal boundaries have the same temperature transient signal. Inset, signal difference between the anisotropic material and its equivalent isotropic material with grain boundaries.

In the TDTR experiment the laser is absorbed in the surface of the transducer and it is Gaussian both in its spatial and temporal dimensions. Thus the boundary condition corresponding to the heat source replicates these characteristics (second line in Eq. (4)). To simplify the simulation, a single pulse of the same duration than the one used in the experiments (8 ps) but with a smaller spatial width ( $4 \mu\text{m} 1/e^2$ ) due limitations in the length of the experimentally characterized layer was simulated. As in the experiment, the value of the maximum intensity of the laser,  $q_0$ , is kept low enough to produce a temperature excursion in the diamond of less than  $1^\circ\text{C}$ . This enabled to linearize the problem by making possible to disregard the impact of the temperature dependence of the thermal properties of the different materials used in the simulation (see Table 1). In this simulation, the temperature on the surface of the Al layer was averaged according to the Gaussian distribution of the heat source, and an example of its output is shown in Fig. 6 for different thermal conductivities and interior boundary conditions of the diamond layer. Note that in this simplified one-pulse simulation the first  $\sim 0.5$  ns of the heat wave are almost independent of the properties of the diamond layer; however when considering a trail of pulses, like in the TDTR experiment, the thermal conductivity of the diamond may impact the composed heat wave earlier making the experiment even more sensitive to the cross-plane

thermal conductivity than the simplified model [27]. From 0.5 ns to  $\sim 4$  ns the transient temperature of an anisotropic layer is almost indistinguishable from an isotropic material having a thermal conductivity equal to its cross-plane thermal conductivity; therefore, the heat wave is completely dominated by the cross-plane thermal conductivity. We want to note that the real size of the laser spot used in the experiment is bigger than in the simulation, and it will result in an even more dominant behavior of the diamond cross-plane thermal conductivity in this region. From 4 ns onward (even later for bigger spot sizes) the in-plane thermal conductivity begins to dominate the heat propagation in the material, and thus it is not interesting. Besides, similarly to what we observed in the in-plane experiment, the transient profiles corresponding to an anisotropic material can be perfectly reproduced by a material with a higher lattice thermal conductivity ( $k_{m\text{-grain}}$ ) but with a thermal resistance between grain boundaries (see Fig. 6, bottom and inset). Finally, we calculated the apparent cross-plane thermal conductivity by fitting the model with internal boundaries with a model without grain boundaries, and as a function of the thermal resistance between grains and for different in-grain thermal conductivities. These results are shown in Fig. 7 together with those obtained in the in-plane simulations.

As expected from the columnar shape of the grains, the in-plane

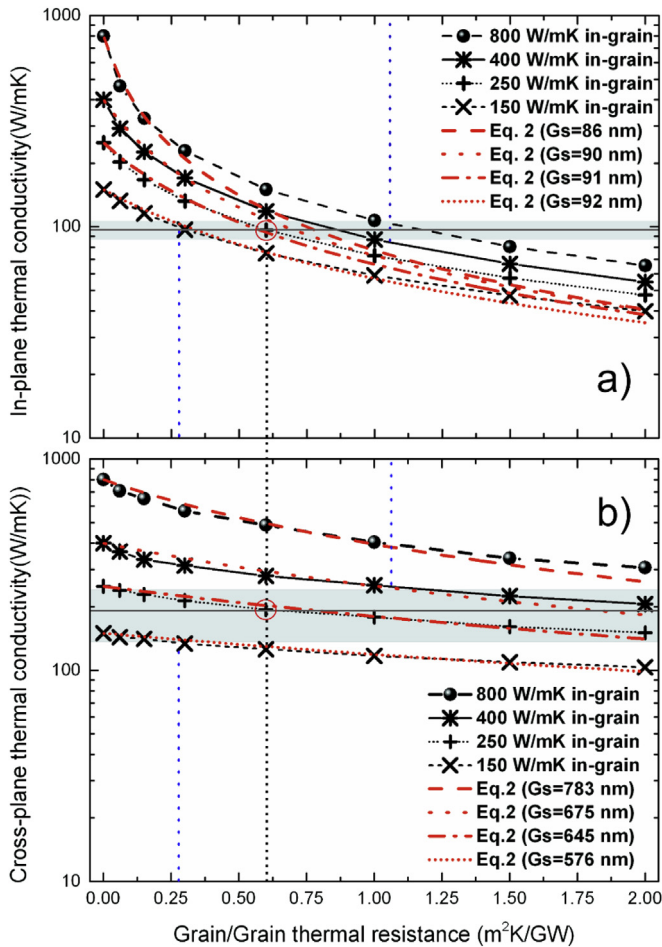


**Fig. 7.** Efficient in-plane (a) and cross-plane (b) thermal conductivity of the 2D slab of diamond shown in Fig. 5 as a function of the grain boundary thermal resistance for different values of the lattice thermal conductivity. The horizontal grey band represents the experimental values including their error band. The simultaneous intersection of the theoretical curves with the average experimental values yields an in-grain thermal conductivity of 250 W/mK and a thermal resistance of 0.625 m<sup>2</sup>K/GW (black dotted line). Blue dotted lines allow to estimate the incertitude of these values. The best fits of Eq. (1) to the results obtained for the 2D slab containing the real grain structure are also shown in the graphs (red curves). (For interpretation of the references to colour in this figure legend, the reader is referred to the web version of this article.)

thermal conductivity of the diamond film is more sensitive to the thermal resistance between grains than the cross-plane thermal conductivity; for an in-grain thermal conductivity of 800 W/mK and a  $R_{GB} = 1 \text{ m}^2\text{K/GW}$  the thin film effective in-plane thermal conductivity drops by a factor 8, while its effective cross plane is only reduced by less than a factor 2 (see Fig. 7). It is also clear from these curves that not all the values of  $(k_{in-grain}, R_{GB})$  which result in an effective in-plane thermal conductivity equal to what was measured are compatible with the measured cross-plane values, and vice versa. Note for instance that while a  $k_{in-grain}$  of 800 W/mK may result in an in-plane thermal conductivity of 95 W/mK when  $R_{GB} = 1.05 \text{ m}^2\text{K/GW}$ , it will require a  $R_{GB}$  well above  $2 \text{ m}^2\text{K/GW}$  for obtaining a cross-plane above 150 W/mK. In fact there is only one set  $(k_{in-grain}, R_{GB})$  of values able to simultaneously fulfill both cross-plane and in-plane measurements, resulting in  $k_{in-grain} = 250 \text{ W/mK}$  and  $R_{GB} = 0.625 \text{ m}^2\text{K/GW}$  respectively (Fig. 7, black dotted line). Nevertheless when the experimental error in the measurements is considered, a range of allowed values rather than a single set of values is obtained. This is shown in Fig. 7 (blue dotted lines) and

allows to estimate the incertitude in  $(k_{in-grain}, R_{GB})$ , resulting in  $150 \text{ W/mK} < k_{in-grain} < 400 \text{ W/mK}$  and  $0.26 \text{ m}^2 \text{ K/GW} < R_{GB} < 1.06 \text{ m}^2 \text{ K/GW}$ . Hence even if the boundaries were completely clean ( $R_{GB} = 0.06 \text{ m}^2\text{K/GW}$ ) the thermal conductivity of this diamond film would not exceed 300 W/mK. Most likely candidates for this reduced thermal conductivity are point defects such as silicon from the substrate and a high density of dislocations. On the other hand the values for  $R_{GB}$  are much higher than the ones calculated for a simple lattice mismatch by molecular dynamics, clearly indicating that there is an accumulation of defects in this region increasing the thermal resistance of the grain boundary.

The curves shown in Fig. 7 also allow testing the validity of the approach given in Eq. (1) for this material. For this, we fitted Eq. (1) to the results obtained in the 2D slab containing the real grain structure value with  $d$  as a single fitting parameter for each  $k_{in-grain}$  (see Fig. 7, red curves). It is observed that for the in-plane thermal conductivity this simple approach is only valid when the value of  $R_{GB}$  is low, and worsens when the lattice conductivity is larger. This is a result of the columnar structure of the diamond film, for which the top half of the film consists of grain boundaries which are in average much further apart than in the bottom half of the film. Thus when the thermal resistance of the boundaries is high enough, the thermal resistance of the bottom part is much higher than in the top part, especially if  $k_{in-grain}$  is high, and the heat flux becomes two dimensional instead of one dimensional. This is not captured by a single grain size in Eq. (1), and results in the underestimation of the in-plane thermal conductivity of the film. This behavior is mitigated for the cross-plane thermal conductivity due to the long grains and their more homogenous size distribution in the XY plane, resulting in a much better fit of Eq. (1) to the results obtained when the real grain structure is considered. Using this approach, the impact of the lattice thermal conductivity and grain boundaries on the commonly reported anisotropy of the thermal conductivity for polycrystalline diamond is summarized in Fig. 8. Here this phenomenon naturally emerges from the polycrystalline grain geometry when the thermal resistance of the grain boundaries is considered; the magnitude of the anisotropy depends on both  $k_{in-grain}$  and  $R_{GB}$  (see Fig. 8-a). For a polycrystalline diamond film with very low lattice defects in its near nucleation site, the anisotropy in thermal conductivity is higher than when the quality of the diamond is low. Even if the grain boundaries are defect-free, the thin polycrystalline diamond film shows a non-negligible anisotropy in its thermal conduction which increases linearly with  $k_{in-grain}$  (Fig. 8-b). It should be noted that in order to include the complexity of the real grain structure of the diamond film we have simplified the complex phonon heat transport in the diamond films to an average diffusive heat transport picture. Thus the physics of the phonon transport inside the diamond grains and across the grain boundaries is lumped in the  $k_{in-grain}$  and  $R_{GB}$  parameters which reflect an average behavior. Using the simplified model implies ignoring any local phenomena – e.g. any local inhomogeneity in the phonon transport in the grains and any local inhomogeneity in the phonon transport across grain boundaries – that can also contribute to the anisotropy. To incorporate a more accurate description of the phonon transport in this material the phonon scattering mechanisms, the phonon MFP confinement in the diamond crystallites, and the frequency dependence of the phonon transport across the grain boundaries must be explicitly considered in the analysis [8,9,33,34]. However, at the best of our knowledge, this can only be carried out using massive molecular dynamics simulations in the reconstructed grain structure of the material, which at the scale of this simulation (tens of microns) will require a prohibitive computation capability. In any case, the diffusive approach used here provides a good average description to unravel the impact of the complex grain structure in the heat

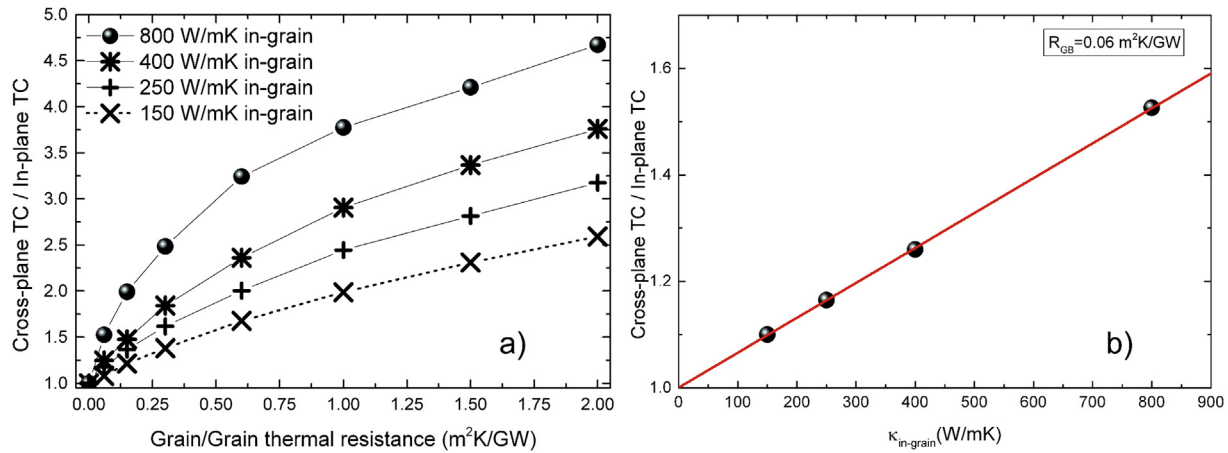


**Fig. 8.** (a) Effective anisotropy of the thermal conductivity of the diamond film as a function of the grain boundary thermal resistance for different values of the diamond lattice thermal conductivity. (b) Effective anisotropy as a function of the lattice thermal conductivity for clean grain boundaries.

transport of this kind of polycrystalline materials.

## 6. Conclusions

The in-plane and cross-plane thermal conductivity of a polycrystalline diamond thin film near its nucleation region were assessed. The grain structure determined by TEM in a long slab of the film was ported to a finite element solver in which the equivalent heat equation corresponding to Raman thermography assisted by  $TiO_2$  nanoparticles and picosecond TDTR thermal measurements performed in the film was solved. With this methodology, we were able to simultaneously quantify the contribution of the lattice and grain boundaries to the total thermal resistance of this material. We found that the lattice thermal conductivity of the near nucleation diamond is 5–8 times smaller than the one observed in IIa single crystals diamonds, clearly indicating the presence of defects inside the grains. On the other hand, we found the thermal resistance between grains much higher than the values computed from molecular dynamic for clean boundaries, evidencing that defects are also accumulated in these boundaries. Finally, we have shown that the anisotropy commonly observed in polycrystalline diamond may be easily explained when the real grain structure is included in the thermal model and that it is expected that this anisotropy increases linearly with the lattice thermal conductivity of the films.

## Acknowledgements

This work is in part supported supported by DARPA Contract No: FA8650-15-C-7517, monitored by Dr. Avram Bar Cohen and Dr. John Blevins supported by Dr. Joseph Maurer and Dr. Abirami. Sivananthan, and by the UK Engineering and Physical Sciences Research Council (EPSRC) under the programme grant GaN-DaME (EP/P00945X/1). MK acknowledges support from the Royal Society and Wolfson Foundation. The authors thank Professor Juan Jimenez (Universidad de Valladolid, Spain), for letting us to use his simulation tools. Any opinions, findings, and conclusions or recommendations expressed in this material are those of the authors and do not necessarily reflect the views of DARPA.

## References

- [1] J.C. Dymant, L.A. D'Asaro, Continuous operation of GaAs junction lasers on diamond heat sinks at 200 °K, *Appl. Phys. Lett.* 11 (1967) 292–294.
- [2] Po Han Chen, Ching Liang Lin, Y.K. Liu, Te Yuan Chung, Cheng-Yi Liu, Diamond heat spreader layer for high-power thin-GaN light-emitting diodes, *IEEE Photonics Technol. Lett.* 20 (2008) 845–847.
- [3] Ali M. Khounsary, T.M. Kuzay, On diamond windows for high power synchrotron x-ray beams, *Nucl. Instrum. Methods Phys. Res. Sect. A Accel. Spectrom. Detect. Assoc. Equip.* 319 (1992) 233–239.
- [4] Yong Han, Boon Long Lau, Xiaowu Zhang, Yoke Choy Leong, Kok Fah Choo, Enhancement of hotspot cooling with diamond heat spreader on Cu micro-channel heat sink for GaN-on-Si device, *IEEE Trans. Compon. Packag. Manuf. Technol.* 4 (2014) 983–989.
- [5] D.J. Twitchen, C.S.J. Pickles, S.E. Coe, R.S. Sussmann, C.E. Hal, Thermal conductivity measurements on CVD diamond, *Diam. Relat. Mater.* 10 (2001) 731–735.
- [6] R.B. Simon, J. Anaya, F. Faili, R. Balmer, G.T. Williams, D.J. Twitchen, M. Kuball, Effect of grain size of polycrystalline diamond on its heat spreading properties, *Appl. Phys. Express* 9 (2016) 061302.
- [7] J.E. Graebner, S. Jin, G.W. Kammlott, B. Bacon, L. Seibles, W. Banholzer, Anisotropic thermal conductivity in chemical vapor deposition diamond, *J. Appl. Phys.* 71 (1992) 5353–5356.
- [8] J. Anaya, S. Rossi, M. Alomari, E. Kohn, L. Tóth, B. Pécz, K.D. Hobart, T.J. Anderson, T.I. Feygelson, B.B. Pate, M. Kuball, Control of the in-plane thermal conductivity of ultra-thin nanocrystalline diamond films through the grain and grain boundary properties, *Acta Mater.* 103 (2016) 141–152.
- [9] J. Anaya, H. Sun, J. Pomeroy, M. Kuball, Thermal management of GaN-on-diamond high electron mobility transistors: effect of the nanostructure in the diamond near nucleation region, in: 15th IEEE Intersociety Conference on Thermal and Thermomechanical Phenomena in Electronic Systems (ITherm), 2016, p. 1558.
- [10] J.G. Felbinger, M.V.S. Chandra, Y. Sun, L.F. Eastman, J. Wasserbauer, F. Faili, D. Babić, D. Francis, F. Ejeckam, Comparison of GaN HEMTs on diamond and SiC substrates, *IEEE Electron. Device Lett.* 28 (2007) 948–950.
- [11] J.W. Pomeroy, M. Bernardoni, D.C. Dumka, D.M. Fanning, M. Kuball, Low thermal resistance GaN-on-diamond transistors characterized by three-dimensional Raman thermography mapping, *Appl. Phys. Lett.* 104 (2014), 083513.
- [12] M. Mohr, L. Daccache, S. Horvat, H.J. Fecht, Influence of grain boundaries on elasticity and thermal conductivity of nanocrystalline diamond films, *Acta Mater.* 122 (2017) 92–98.
- [13] H. Verhoeven, A. Flöter, H. Reiß, R. Zachai, D. Wittorf, W. Jäger, Influence of the microstructure on the thermal properties of thin polycrystalline diamond films, *Appl. Phys. Lett.* 71 (1997) 1329–1331.
- [14] K.E. Goodson, Y.S. Ju, Heat conduction in novel electronic films, *Annu. Rev. Mater. Sci.* 29 (1999) 261–293.
- [15] S. Aditya, J. Cho, K.D. Hobart, T.I. Feygelson, B.B. Pate, M. Asheghi, D.G. Cahill, K.E. Goodson, Anisotropic and inhomogeneous thermal conduction in suspended thin-film polycrystalline diamond, *J. Appl. Phys.* 119 (2016) 175103.
- [16] P.K. Bachmann, H.J. Hagemann, H. Lade, D. Leers, D.U. Wiechert, H. Wilson, D. Fournier, K. Plamann, Thermal properties of C/H-, C/H/O-, C/H/N- and C/H/X-grown polycrystalline CVD diamond, *Diam. Relat. Mater.* 4 (1995) 820–826.
- [17] M. Nazari, B.L. Hancock, J. Anderson, A. Savage, E.L. Piner, S. Graham, F. Faili, S. Oh, D. Francis, D. Twitchen, M. Holt, Near-ultraviolet micro-Raman study of diamond grown on GaN, *Appl. Phys. Lett.* 108 (2016), 031901.
- [18] X. Zhou, G.D. Watkins, R.K. McNamara, R.P. Messmer, S. Chawla, Hydrogen-related defects in polycrystalline CVD diamond, *Phys. Rev. B* 54 (1996) 7881–7890.
- [19] S. Michaelson, O. Ternyak, A. Hoffman, Y. Lifshitz, Correlation between diamond grain size and hydrogen retention in diamond films studied by scanning electron microscopy and secondary ion mass spectroscopy, *Appl. Phys. Lett.* 90 (2007), 031914.

- [20] D. Spiteri, J. Anaya, M. Kuball, The effects of grain size and grain boundary characteristics on the thermal conductivity of nanocrystalline diamond, *J. Appl. Phys.* 119 (2016), 085102.
- [21] M.A. Angadi, T. Watanabe, A. Bodapati, X. Xiao, O. Auciello, J.A. Carlisle, J.A. Eastman, P.K. Schelling, S.R. Phillpot, Thermal transport and grain boundary conductance in ultrananocrystalline diamond thin films, *J. Appl. Phys.* 99 (2006), 114301.
- [22] J. Anaya, S. Rossi, M. Alomari, E. Kohn, L. Tóth, B. Pécz, M. Kuball, Thermal conductivity of ultrathin nano-crystalline diamond films determined by Raman thermography assisted by silicon nanowires, *Appl. Phys. Lett.* 106 (2015), 223101.
- [23] Y.L. Du, Y. Deng, M.S. Zhang, Variable-temperature Raman scattering study on anatase titanium dioxide nanocrystals, *J. Phys. Chem. Solids* 67 (2006) 2405–2408.
- [24] W.F. Zhang, Y.L. He, M.S. Zhang, Z. Yin, Q. Chen, Raman scattering study on anatase TiO<sub>2</sub> nanocrystals, *J. Phys. D* 33 (2000) 912–916.
- [25] N. Lundt, S.T. Kelly, T. Rödel, B. Remez, A.M. Schwartzberg, M. Adam, A. Ceballos, C. Baldasseroni, P.A.F. Anastasi, M. Cox, F. Hellman, S.R. Leone, M.K. Gilles, High spatial resolution Raman thermometry analysis of TiO<sub>2</sub> microparticles, *Rev. Sci. Instrum.* 84 (2013) 104906.
- [26] D.G. Cahill, Analysis of heat flow in layered structures for time-domain thermoreflectance, *Rev. Sci. Instrum.* 75 (2004) 5119–5122.
- [27] A.J. Schmidt, X.Y. Chen, G. Chen, Pulse accumulation, radial heat conduction, and anisotropic thermal conductivity in pump-probe transient thermoreflectance, *Rev. Sci. Instrum.* 79 (2008), 114902.
- [28] J. Liu, J. Zhu, M. Tian, X. Gu, A. Schmidt, R. Yang, Simultaneous measurement of thermal conductivity and heat capacity of bulk and thin film materials using frequency-dependent transient thermoreflectance method, *Rev. Sci. Instrum.* 84 (2013), 034902.
- [29] D.G. Cahill, F. Watanabe, Thermal conductivity of isotopically pure and Ge-doped Si epitaxial layers from 300 to 550 K, *Phys. Rev. B* 70 (2004), 235322.
- [30] T.L. Bougher, L. Yates, C.-F. Lo, W. Johnson, S. Graham, B.A. Cola, Thermal boundary resistance in GaN films measured by time domain thermoreflectance with robust Monte Carlo uncertainty estimation, *Nanoscale Microscale Thermophys. Eng.* 20 (2016) 22–32.
- [31] K.E. Goodson, O.W. Käding, M. Rösner, R. Zachai, Thermal conduction normal to diamond-silicon boundaries, *Appl. Phys. Lett.* 66 (23) (1995) 3134–3136.
- [32] M. Battabyal, O. Beffort, S. Kleiner, S. Vaucher, L. Rohr, Heat transport across the metal–diamond interface, *Diam. Relat. Mater.* 17 (7) (2008) 1438–1442.
- [33] G. Chen, Thermal conductivity and ballistic-phonon transport in the cross-plane direction of superlattices, *Phys. Rev. B* 57 (23) (1998) 14958.
- [34] Z. Wang, J.E. Alaniz, W. Jang, J.E. Garay, C. Dames, Thermal conductivity of nanocrystalline silicon: importance of grain size and frequency-dependent mean free paths, *Nano Lett.* 11 (6) (2011) 2206–2213.